Formation of One-Dimensional Electronic States along the Step Edges of $CeO_2(111)$

Niklas Nilius,[†,*] Sergey M. Kozlov,[‡] Jan-Frederick Jerratsch,[†] Martin Baron,[†] Xiang Shao,[†] Francesc Viñes,[‡] Shamil Shaikhutdinov,[†,*] Konstantin M. Neyman,[‡,§,*] and Hans-Joachim Freund[†]

[†]Fritz-Haber-Institut der Max-Planck-Gesellschaft, Faradayweg 4-6, 14195 Berlin, Germany, [‡]Departament de Química Física, Universitat de Barcelona, C/Martí i Franquès 1, 08028 Barcelona, Spain, and [§]Institució Catalana de Recerca i Estudis Avançats (ICREA), 08010 Barcelona, Spain

ABSTRACT

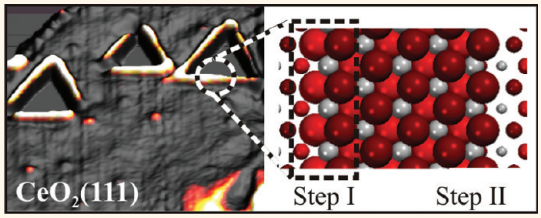

Scanning tunneling microscopy (STM) combined with density functional theory (DFT) are used to analyze the structural and electronic properties of step edges on the surface of $CeO_2(111)$ films grown on Ru(0001). Depending on the preparation conditions, ⟨211⟩ or ⟨110⟩-oriented steps develop on the surface, which results in the formation of ceria ad-islands with hexagonal or triangular shapes. STM conductance spectroscopy reveals pronounced differences in the electronic properties of the step edges, as reflected in different onset positions of the ceria conduction band. The band shifts are related to the development of distinct edge electronic states that split-off from the ceria conduction band, as shown with DFT calculations. The separation of the edge states from the main band is governed by the atom-coordination and local charge-distribution along the edge, the latter giving rise to the development of electrostatic dipoles. We expect that the observed edge morphologies determine not only the electronic properties but also the adsorption behavior of step edges on the $CeO_2(111)$ surface.

KEYWORDS: ceria · step edges · electronic properties · edge polarity · STM · DFT

Cerium dioxide plays an important role in heterogeneous catalysis, both as active material and support.[1−4] Its outstanding redox properties rely on two closely related aspects. First, ceria exhibits a particularly low formation energy for oxygen vacancies, which renders lattice oxygen available in chemical reactions.[5−7] Second, ceria is a good electron acceptor, as the initially empty Ce 4f states can be filled up with electrons, thereby reducing the charge state of respective Ce ions from +4 to +3.[8] The latter effect facilitates electron transfer from suitable adspecies into the oxide surface, promoting the chemical activity of the material.[4,9]

Naturally, defects and low-coordinated sites in the ceria surface are most susceptible to reduction processes and therefore strongly involved in the oxide chemistry. This has been demonstrated in a number of recent experiments that revealed a higher catalytic activity for defect-rich ceria nanoparticles with respect to the extended surface.[10−13] Moreover, one-dimensional (1D) defects, that is, step edges and dislocation lines, have been identified as preferred nucleation sites for metal particles.[14] The specific properties of such defects have several reasons. Naturally, atoms along step edges and grain boundaries are characterized by a reduced number of nearest neighbors, which renders them susceptible to desorption[15] and explains the small vacancy-formation energies.[16] A reduced atom-coordination also alters the electronic structure of line defects, being characterized by split-off and 1D electronic states that are not present in the bulk.[17−20] In addition, the geometric distortions that are exerted in the ceria lattice by converting Ce^{4+} into more spacious Ce^{3+} ions are better accommodated at step edges than in the ideal surface.[6,21,22] Another, widely disregarded point concerns the charge imbalance that is produced in an ionic crystal by certain defects. The (111) surface of ceria comprises alternating layers of cations and anions and belongs to type II polar terminations according to Tasker's scheme.[23,24] Whereas O^{2-}−Ce^{4+}−O^{2-} trilayers, being the regular (111) building blocks, are fully charge compensated, any perturbation of this configuration may induce a dipole moment. Given the large energies associated with polar structures, the contribution of such defects to the surface free-energy and hence the chemical properties of ceria might be substantial.[23]

* Address correspondence to nilius@fhi-berlin.mpg.de, shaikhutdinov@fhi-berlin.mpg.de, konstantin.neyman@icrea.es.

Received for review September 22, 2011 and accepted December 29, 2011.

Published online December 29, 2011
10.1021/nn2036472

In this work, we have analyzed the topographic and electronic structure of step edges on the CeO_2(111) surface, using a combined scanning tunneling microscopy (STM) and density functional theory (DFT) approach. Whereas a detailed geometric characterization of the ceria steps has been reported in a recent atomic-force microscopy study,[25] no information on their electronic structure has been provided so far. Here, we demonstrate that step edges on the CeO_2(111) surface have unusual electronic and electrostatic properties that might be decisive for the adsorption and reaction behavior of this particular oxide.

RESULTS AND DISCUSSION

Step Morphologies. Large-scale STM images of crystalline CeO_2(111) films exhibit two kinds of step edges (Figure 1a). The first one delimits wide, atomically flat terraces and originates from steps in the underlying Ru(0001) support. The second type borders hexagonal ad-islands and pits that develop during oxide growth. We will focus our discussion to the latter type that is intrinsic to the ceria lattice. Step edges surrounding the ceria ad-islands have the typical height of one O−Ce−O trilayer (0.31 nm), indicating that the (111) surface develops a sole termination. Depending on the preparation conditions, two prevalent step orientations are observed:

(i) Low temperature films (T_{anneal} < 1000 K) develop two ⟨110⟩-oriented edge types that run along the high-symmetry axes of the ceria lattice and have opposite descents (Figure 1b). In both cases, the spacing between the edge atoms amounts to 0.382 nm, which matches the bulk lattice constant of ceria.[26] The length ratio between the two step types was found to vary with annealing temperature of the film. Whereas at 1000 K, one step type is roughly two times longer than the other, producing islands with truncated triangular shape (Figure 1b), the two edges are equally long at 900 K and the islands become hexagonal.[25] The orientation of the triangular islands inverts when crossing a step edge or domain boundary in the film, suggesting that the respective step type changes position within the island (Figure 1a).

(ii) The second step type runs along ⟨211⟩ directions of the oxide lattice and preferentially develops at annealing temperatures above 1000 K (Figure 1c). In accordance with the 30° rotation with respect to the ⟨110⟩ edges, the spacing of the edge atoms is larger by a factor of $\sqrt{3}$ (0.67 nm). Only one step configuration is observed in this case and all ad-islands are therefore of hexagonal shape.

On the basis of the orientation and topographic appearance of step edges in the experiment, we have searched for corresponding structure models by means of total energy calculations. Out of various considered configurations, we have concentrated on those that are characterized by low formation energies and have the stoichiometry of bulk ceria.[16] Optimized ⟨110⟩-oriented steps either comprise down-sloping O−O units perpendicular to the edge direction (Figure 2a, left) or display a concave shape with the outermost atom row being an O-row in the topmost atomic plane (Figure 2a, center). Following the established notation for step edges on the iso-structural CaF_2(111) surface,[27−29] we refer to the two step configurations as type I (positive descent) and type II (negative descent) in the following. While the positive descent of the type I edge corresponds to a (110) nanofacet, the type II descent resembles a (111) plane. The two step types can also be distinguished *via* their normal-vectors within the surface, which run along

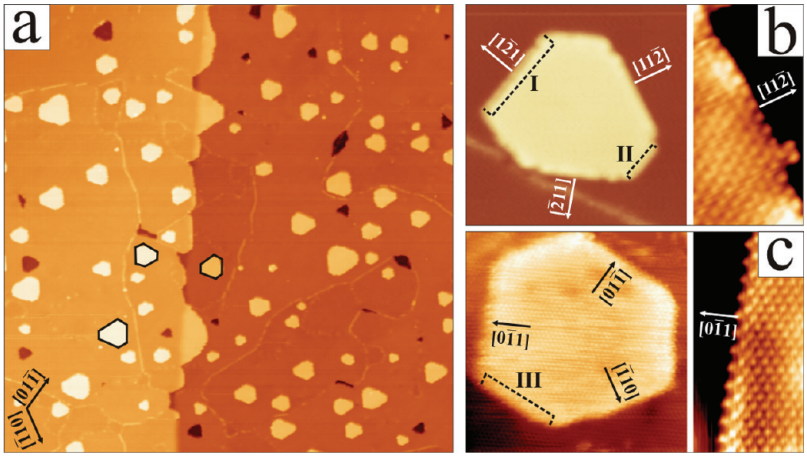

Figure 1. (a) STM image showing the CeO_2/Ru(0001) film-morphology after annealing to a maximum temperature of 1000 K (U_S = 3.0 V, 280 × 280 nm^2). All islands are delimited by type I and II steps and invert their shape when crossing a domain boundary or step edge. (b) Close-up images of a truncated triangular I/II island (20 × 20 nm^2) and a type I step shown with atomic resolution (6 × 3 nm^2). (c) STM images of a hexagonal island bordered by type III steps (20 × 20 nm^2) and the same step type shown with atomic resolution (10 × 5 nm^2). The corresponding normal-vectors are indicated in the figures.

[11$\bar{2}$], [1$\bar{2}$1], or [$\bar{2}$11] directions for type I edges and along [$\bar{1}\bar{1}$2], [$\bar{1}$2$\bar{1}$], or [2$\bar{1}\bar{1}$] for type II.

The crystallographic reason for the occurrence of two inequivalent ⟨110⟩ steps is that the corresponding plane perpendicular to the surface is not a symmetry plane of the fluorite lattice. This also explains why the relative step positions within a given island change when going from one trilayer to the next (Figure 1a). The fact that the island shape inverts also when crossing a domain boundary suggests that two stacking-domains with a reversed sequence of the oxygen planes (ABC and CBA) are present in our films. The observed temperature-driven changes from triangular to hexagonal island shapes, on the other hand, reflect the different thermodynamic stabilities of type I and II steps, which will be discussed in a forthcoming paper.

As the ⟨211⟩-oriented steps follow a symmetry plane of the fluorite lattice, only one step type is revealed in this case (Figure 2b). The energetically favored structure has a vertical descent and all planes of the O−Ce−O trilayer terminate at the same position. The normal vector of ⟨211⟩ steps points to one of the equivalent ⟨$\bar{1}$10⟩ directions and the respective nanofacet is a ($\bar{1}$10)-type of plane. We will refer to these steps as type III in the following. We note again that only stoichiometric step configurations have been considered here due to computational limitations. Potential nonstoichiometric models can be found in the literature.[16,25]

Electronic Properties of Step Edges: Experimental Results. The easiest way to explore the electronic structure of the ceria step edges is the acquisition of bias-dependent STM images, as shown for type I and II steps in Figure 3. None of the exposed edges feature a particular contrast at small positive bias, when electrons tunnel from the tip into the empty f-states of ceria.[30,31] This situation changes above 4.0 V when the longer steps of the quasi hexagonal islands (assigned to type I) and sections of the domain boundaries start to appear bright. This contrast enhancement gives a first hint on the different electronic nature of line defects with respect to the flat CeO_2 surface. Differential conductance (d*I*/d*V*) maps that directly probe the availability of electronic states at a given bias provide deeper insight into the state-density along the step edges. A corresponding image series is shown in Figure 4a for quasi-hexagonal islands bordered by longer type I and shorter type II steps. Below 4.0 V, no topographic contrast is revealed for the island edges as compared to the interior, whereas the simultaneously taken d*I*/d*V* map already features an enhanced edge-signal due to a new, yet weak conductance channel. Above 4.0 V, the type I steps exhibit a sharp increase of their apparent height that is absent for type II steps and imprints a distinct 3-fold symmetry onto the actually hexagonal islands. In the d*I*/d*V* maps, the contrast maximum shifts from the step edges to the flat surface, suggesting that the new transport channel becomes available there as well. At even higher bias (4.4 V), the contrast enhancement of type I steps diminishes again in the topographic channel and the d*I*/d*V* maximum shifts from the flat surface to the interior of the spatially confined islands. The described contrast evolution is

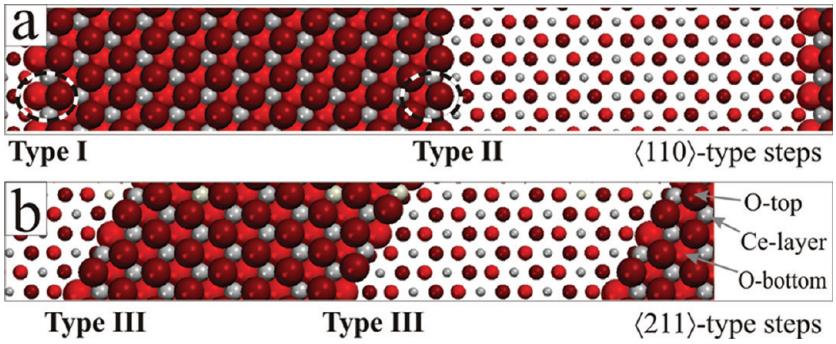

Figure 2. (a) DFT structure model of a CeO_2(111) trilayer stripe exposing type I (left) and type II steps (center). Typical building blocks of the steps are marked by dashed ovals. (b) Structure model of a trilayer stripe delimited by type III steps.

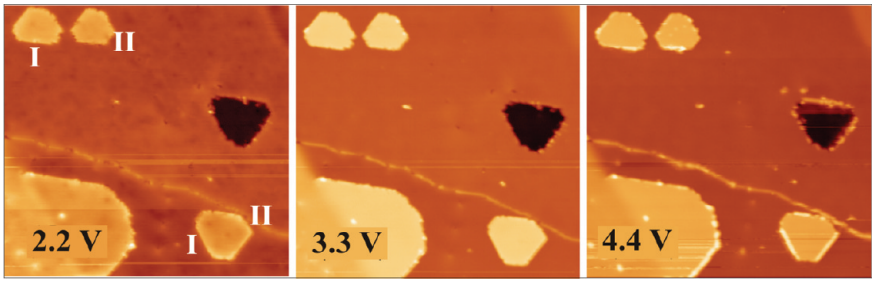

Figure 3. STM topographic images of the ceria surface exposing type I and II steps at three different bias voltages (65 × 65 nm^2). Note the bright appearance of type I steps and lines defects at 4.4 V sample bias.

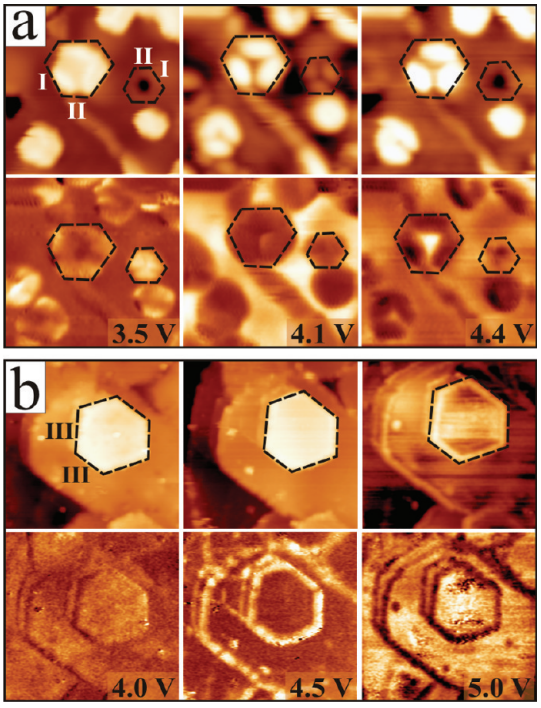

Figure 4. Topographic (upper row) and conductance images (lower row) of ceria ad-islands and holes exposing (a) type I/II and (b) type III steps. The images are 25 × 25 nm^2 in panel a and 45 × 45 nm^2 in panel b and have been taken at the indicated bias voltages.

not specific to the edges of ceria ad-islands, but occurs in a similar fashion for trilayer-deep holes and grain boundaries (Figure 4a). Also there, certain fractions of the line defects turn bright at relatively low bias, indicating a similar electronic structure.

Ceria islands terminated by type III steps show a comparable behavior, only that the threshold bias at which the contrast change occurs is higher. Below 4.5 V, the inner part of the ad-islands and surrounding step edges appear with the same topographic height, while a characteristic brim becomes visible in the accompanying d*I*/d*V* maps (Figure 4b). Again, the signal enhancement at the edges emerges first in the conductance channel, while the topographic signature only follows at 0.5 V higher bias. This offset reflects the integrating nature of STM images, where all electronic states between a preset sample bias and the Fermi level contribute to the detected contrast.

The presence of distinct electronic states along type I ceria step edges is confirmed with d*I*/d*V* spectra taken in the region of the conduction band (Figure 5). Apart from a small peak at 2.3 V that marks the empty Ce 4f states,[30] no conductance signal is detected below 3.5 V in agreement with the large oxide band gap. Surprisingly, the conduction-band onset that shows up as pronounced maximum is reached at different energies depending on the surface position selected for spectroscopy. The lowest onset is detected for type I step edges (3.6 V), in correspondence with their bright

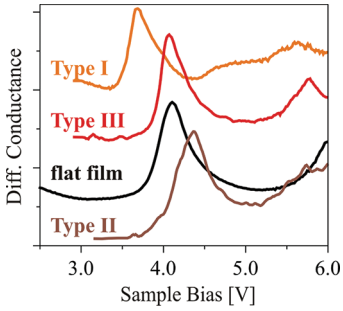

Figure 5. Differential conductance spectra taken at different step edges and the flat CeO_2(111) surface with enabled feedback loop.

appearance in topographic images taken in this bias range. The flat surface and type III edges follow at around 4.1 V and the highest onset position (4.4 V) is found for type II steps that indeed remain featureless in the topographic images. It is this spatial variation in the conduction-band onset that is responsible for the distinct bias-dependent contrast of ceria step edges in the STM. We note that d*I*/d*V* spectroscopy can only provide an approximate value of the band onset, as the oxide states experience a slight upshift in the tip-induced electric field. However, relative changes in the band positions are reliably determined in the experiment.

Electronic Properties of Step Edges: Results of the DFT Calculations. To analyze the nature of electronic states emerging on the ceria step edges, we have calculated their LDOS using the structure models shown in Figure 2. The lowest unoccupied states are the Ce 4f orbitals at 2.5 eV above the valence-band edge, that is, inside the fundamental gap. The conduction band is reached at around 5.0 eV (Figure 6), a value that slightly depends on the size of the considered system and the proximity to adjacent step edges. On the regular (111) surface, the states at the band onset have Ce 5d character with a small 6sp contribution; however this picture changes at the step edges. Along type I steps, new states with notable sp contribution occur at 0.6 eV below the conduction-band onset. Similar states are found along type III steps, only their energy splitting from the main band is just 0.15 eV. A significant sp contribution and energy position below the main band renders these split-off states particularly important for electron tunneling into the step edges. This relevance becomes immediately clear from the simulated STM images, as shown for the different edge types in Figure 7. Below the conduction band onset, that is, inside the gap, the topographic contrast is entirely governed by the true height difference between the ad-island and the oxide surface and the step edges remain featureless. At 4.5 V, the type I step appears bright because its split-off band becomes available for tunneling. The contrast enhancement vanishes above 5.0 V, when the regular conduction band is reached on type II steps and the flat surface as well. A similar behavior is revealed for

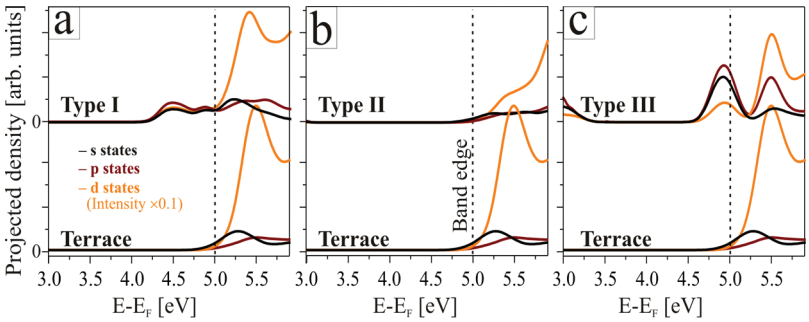

Figure 6. Calculated density of *s*, *p*, and *d*-states along the different step edges and the flat ceria surface. The split-off states below the conduction band onset are clearly visible for type I and III steps.

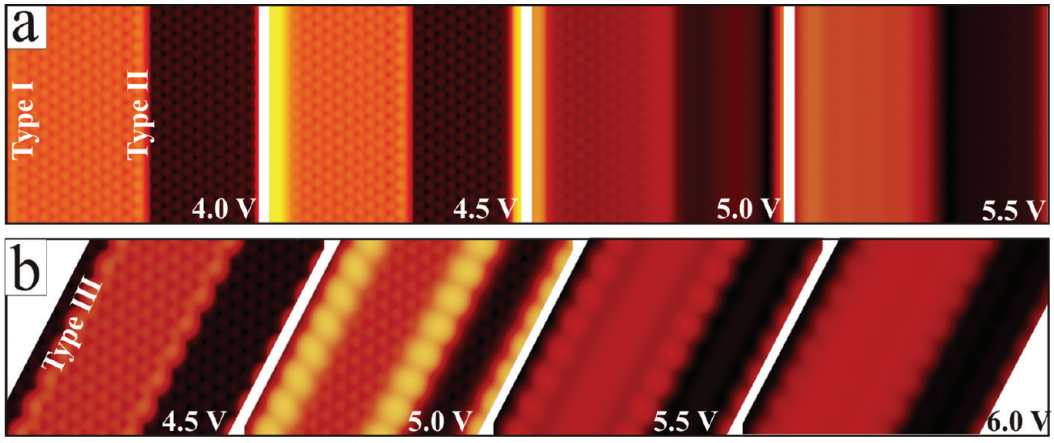

Figure 7. Simulated STM images for (a) type I/II and (b) type III step edges. Depending on the bias voltage, the type I and III step edges appear bright with respect to the flat surface.

type III steps, which also appear with their true topographic height for bias values inside the gap, but turn bright once the edge states are reached at 5.0 V. The split-off states identified in the DFT calculations thus provide a plausible explanation for the distinct edge contrast observed in the STM. Their presence is also compatible with the lower conductance onset revealed for type I steps in the d*I*/d*V* spectra shown in Figure 5.

Discussion. In this section, we will address the structural and electrostatic peculiarities of the ceria step edges that are responsible for the development of the split-off states. The most obvious deviation from he flat surface is the lower coordination number of the step atoms. Whereas Ce ions along type I and II steps are six-fold coordinated (compared to seven-fold in the flat surface), this number reduces to five at type III edges. A smaller coordination number weakens the Madelung potential and lowers its symmetry at the edge, which in turn affects the local gap size. This influence has been explored for the Ce d states that experience a symmetry-dependent energy shift. On type I steps, mainly the d(*xz*) and d(z^2) orbitals are stabilized, whereas on type III steps the d(*xy*), d(*xz*), and d(x^2-y^2) states appear at reduced energy. Furthermore, an asymmetric Madelung potential is incompatible with the intrinsic inversion symmetry of d levels, which explains why the split-off states have a pronounced sp character. The role of the Madelung potential on the local gap-size has been previously discussed for step edges in the MgO(001) surface.[32,33]

A reduced coordination number at the edge also induces qualitative changes in the chemical bonding between cations and anions. Whereas ionic contributions are strengthened in a dense-packed lattice, covalent interactions gain importance among undercoordinated atoms and ions. Such modifications in the binding character can be probed by the Bader charges calculated for the different step configurations.[34] Indeed, the absolute charges of Ce and O ions are slightly reduced by up to 0.1e at the step with respect to the ideal surface (Ce: +2.35e, O: −1.2e), indicating a larger covalent contribution. The more covalent character of the bonds results in the formation of mixed Ce−O states that may be displaced from the main bands. Such a splitting of discrete states from a bulk continuum is a common phenomenon and has been observed for surfaces and step edges of various metallic, semiconducting, and insulating materials.[17,20,35,36] The split-off states revealed here are therefore fully compatible with the concept of 1D edge states.

Although the occurrence of distinct edge states may be rationalized by the deviating binding properties

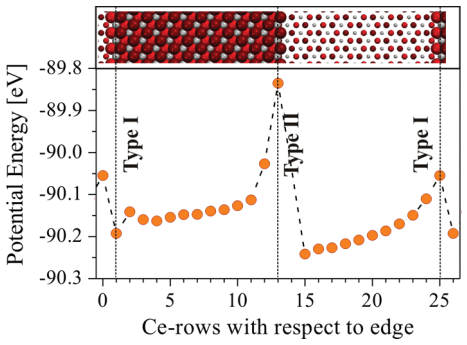

Figure 8. Electrostatic potential energy of a probe electron in a Ce ion at different distances from type I/II step edges. The potential course reflects the repulsive/attractive forces induced by negative/positive excess charges at different positions of the step edge. A corresponding structure model is shown in the top panel.

along the ceria steps, their energy positions is governed by another parameter that is the local charge distribution. CeO_2(111), as a layered ionic material, is particularly susceptible to polarity effects, as defects often break the charge balance within the surface O−Ce−O trilayer.[23] In general, an accumulation of positive charges leads to a stabilization of the oxide electronic states and lowers their energy, while extra electrons push the oxide bands upward. The largest perturbation in the charge balance occurs on type I steps, which feature a positive descent with the O-top plane terminating earlier than the O-bottom plane (Figure 2a). This gives rise to a lack of negative charges at the top of the edge and an electron accumulation at its bottom, producing a positive electrostatic dipole pointing toward the vacuum. As sketched above, such a charge distribution stabilizes the electrons and leads to a rigid shift of the edge electronic states to lower energies. The magnitude of this effect is derived from the calculated potential energy experienced by an electron in a Ce ion at different distances from the edge (Figure 8). When approaching a type I edge from the upper terrace, the potential energy first decreases before it jumps to higher values once the step is passed. This potential switch reflects the stabilizing effect of the positive charges at the top of step I followed by a destabilization due to the excess electrons at its bottom. The strength of the associated dipole moment projected onto the surface normal μ_z can be estimated with: $\mu_z = \sum q_i z_i$. Using the computed ion charges and vertical positions, q_i and z_i, the dipole moment at the type I step is determined to be +1.2 D per CeO_2 unit. This edge dipole is the main reason for the down-shift of the type I split-off states.

The type II steps with their negative decent exhibit the opposite trend, as extra charges accumulate in the top plane and the resulting dipole points away from the vacuum ($\mu_z = -1.1$D). As a result, the edge states move toward higher energy, merging with the main conduction band, and the electrostatic energy rises when approaching the step from the upper terrace. The absence of low-lying split-off states in this case is reflected in the dark appearance of type II steps, both in topographic and conductance images. Finally, the type III steps have the most compact configuration and are nearly dipole compensated ($\mu_z = +0.04$ D). The energy position of the split-off states is therefore mainly determined by the low coordination number of the edge ions, while electrostatic contributions play a negligible role. In fact, the good polarity compensation of type III steps might be responsible for a preferred development at high temperature, where low-energy and nonpolar configurations become favored.

CONCLUSIONS

STM imaging and spectroscopy revealed distinct differences in the electronic structure of ceria step edges with respect to the perfect (111) surface. Three kinds of trilayer steps have been identified, which differ in their orientation, in the inclination of the associated nanofacet and the local charge distribution. One of them, the type I step, stands out as it appears bright in low-bias STM images and has a downshifted conduction band onset in d*I*/d*V* spectra. Density functional GGA+U calculations ascribed this experimental finding to the formation of edge-electronic states that are displaced from the main conduction band of ceria. The split-off states have significant sp contribution and therefore dominate the tunneling into the step edges at low sample bias. The edge electronic states develop due to a lower atom-coordination number and a more covalent nature of bonds along the step edges. A sizable electrostatic dipole at type I steps further promotes the splitting of the respective states from the main band.

The peculiar electronic structure in combination with an uncompensated edge-dipole will largely affect the adsorption behavior of ceria step edges and might provide an explanation for the high chemical activity of ceria nanoislands.[3,4] We will explore this issue in future studies that address the interaction of adsorbates with the different step types. Also, the dominance of specific step edges at certain preparation conditions calls for additional experiments, as this might open an interesting route to alter the chemical properties of CeO_2-(111) by tuning the step morphology.

METHODS

The experiments were performed in an ultrahigh vacuum chamber equipped with a custom-built Beetle-type STM operated at 10 K. While imaging was accomplished in the constant current mode ($I = 5$ pA), the electronic properties were deduced from differential conductance (d*I*/d*V*) measurements

performed with a lock-in amplifier. The ceria film was prepared by depositing a Ce wetting layer in 10^{-6} mbar O_2 onto the O(2 × 1) Ru(0001) surface at 100 K.[37,38] After an increase in the temperature to 700 K, additional Ce was dosed at constant O_2 pressure, and the sample was finally annealed to temperatures between 900 and 1100 K for 10 min. The procedure resulted in the formation of crystalline and atomically flat CeO_2(111) films, as concluded from STM images and low-energy-electron-diffraction data displaying a sharp (1.4 × 1.4) pattern with respect to the substrate spots. The average film thickness was determined to be six O−Ce−O trilayers (1.8 nm), using the attenuation of the Ru 3d signal in X-ray photoelectron spectroscopy.

To gain theoretical insight into the properties of ceria step edges, spin-restricted DFT calculations were performed with the VASP code,[39,40] using the generalized gradient approximation and the PW91 exchange-correlation functional.[41] Test calculations including spin-degrees of freedom gave similar results. In accordance with earlier studies, the Hubbard correction scheme[42] with U_{eff} = 4 eV was applied to reinforce the localization of the Ce 4f orbitals.[43,44] The core−valence interaction was treated with the projector augmented wave method,[45] setting the energy cutoff to 415 eV. The local density of states (LDOS) was computed with dense (1 × 11 × 1) and (1 × 7 × 1) Monkhorst grids, while structural optimization was performed with a (1 × 3 × 1) grid. As the Fermi level in an insulating system depends on both defect structure and temperature, all energies are given with respect to the valence band edge, that is, the highest occupied state of the system. The STM images were simulated with the Tersoff−Hamann approach.[46] The different step edges were modeled with stoichiometric O−Ce−O stripes located on top of a double-trilayer thick CeO_2(111) slab. To minimize mutual interactions between the steps, relatively large unit cells were used that consist of 61 Ce and 122 O atoms (top layer, $Ce_{13}O_{26}$; second and third trilayer, $Ce_{24}O_{48}$ each). The ⟨110⟩-oriented steps were modeled with a rectangular 7.935 × 0.382 nm^2 supercell, while ⟨211⟩ steps were described with a rhombic 5.291 × 0.661 nm^2 cell. The slabs were separated by 1.7 nm of vacuum from their nearest periodic image. The topmost trilayers were relaxed during geometry optimization until atomic forces decreased to 0.15 eV/nm, whereas the bottom trilayer was kept at its bulk position. The potential energy of a trial electron was calculated by using spatial charge-density distributions without assigning the electron density to specific atoms.

Acknowledgment. The authors acknowledge financial support from the Cluster of Excellence `UNICAT' through the German Science Foundation, the Spanish MICINN (grant FIS2008-02238), and the Generalitat de Catalunya (Grants 2009SGR1041 and XRQTC). S. Kozlov is grateful to the Spanish Ministerio de Educación for a predoctoral FPU research fellowship AP2009-3379. F. Viñes thanks the MICINN for a postdoctoral *Juan de la Cierva* grant (JCI-2010-06372).

Supporting Information Available: Discussion of the atom relaxation along different step edges; introduction of alternative step configurations. This material is available free of charge *via* the Internet at http://pubs.acs.org.

REFERENCES AND NOTES

1. Trovarelli, A. *Catalysis by Ceria and Related Materials*; Imperial College Press: London, 2002.
2. Fu, Q.; Saltsburg, H.; Flytzani-Stephanopoulos, M. Active Nonmetallic Au and Pt Species on Ceria-Based Water−Gas Shift Catalysts. *Science* **2003**, *301*, 935.
3. Yang, F.; Graciani, J.; Evans, J.; Liu, P.; Hrbek, J.; Fdez. Sanz, J.; Rodriguez, J. A. CO Oxidation on Inverse CeO(*x*)/Cu(111) Catalysts: High Catalytic Activity and Ceria-Promoted Dissociation of O_2. *J. Am. Chem. Soc.* **2011**, *133*, 3444–3451.
4. Vayssilov, G. N.; Lykhach, Y.; Migani, A.; Staudt, T.; Petrova, G. P.; Tsud, N.; Skála, T.; Bruix, A.; Illas, F.; Prince, K. C.; *et al.* Support Nanostructure Boosts Oxygen Transfer to Catalytically Active Platinum Nanoparticles. *Nat. Mater.* **2011**, *10*, 310.
5. Nolan, M.; Parker, S. C.; Watson, G. W. The Electronic Structure of Oxygen Vacancy Defects at the Low Index Surfaces of Ceria. *Suf. Sci.* **2005**, *595*, 223.
6. Ganduglia-Pirovano, M. V.; Da Silva, J. L.; Sauer, J. Density-Functional Calculations of the Structure of Near-Surface Oxygen Vacancies and Electron Localization on CeO_2(111). *Phys. Rev. Lett.* **2009**, *102*, 026101.
7. Migani, A.; Vayssilov, G. N.; Bromley, S. T.; Illas, F.; Neyman, K. M. Greatly Facilitated Oxygen Vacancy Formation in Ceria Nanocrystallites. *Chem. Commun.* **2010**, *46*, 5936–5938.
8. Skorodumova, N. V.; Simak, S. I.; Lundqvist, B. I.; Abrikosov, I. A.; Johansson, B. Quantum Origin of the Oxygen Storage Capability of Ceria. *Phys. Rev. Lett.* **2002**, *89*, 166601.
9. Baron, M.; Abbott, H.; Bondarchuk, O.; Stacchiola, D.; Uhl, A.; Shaikhutdinov, S.; Freund, H. J.; Popa, C.; Ganduglia-Pirovano, M. V.; Sauer, J. Resolving the Atomic Structure of Vanadia Monolayer Catalysts: Monomers, Trimers, and Oligomers on Ceria. *Angew. Chem., Int. Ed.* **2009**, *48*, 8006.
10. Carrettin, S.; Concepcion, P.; Corma, A.; Nieto, J. M. L.; Puntes, V. F. Nanocrystalline CeO_2 Increases the Activity of Au for CO Oxidation by Two Orders of Magnitude. *Angew. Chem., Int. Ed.* **2004**, *43*, 2538–2540.
11. Guzman, J.; Carrettin, S.; Corma, A. Spectroscopic Evidence for the Supply of Reactive Oxygen during CO Oxidation Catalyzed by Gold Supported on Nanocrystalline CeO_2. *J. Am. Chem. Soc.* **2005**, *127*, 3286–3287.
12. Murugan, B.; Ramaswamy, A. V. Defect-Site Promoted Surface Reorganization in Nanocrystalline Ceria for the Low-Temperature Activation of Ethylbenzene. *J. Am. Chem. Soc.* **2007**, *129*, 3062–3063.
13. Hsiao, W. I.; Lin, Y.-S.; Chen, Y.-C.; Lee, C.-S. The Effect of the Morphology of Nanocrystalline CeO_2 on Ethanol Reforming. *Chem. Phys. Lett.* **2007**, *441*, 294–299.
14. Lu, J.-L.; Gao, H.-J.; Shaikhutdinov, S.; Freund, H.-J. Morphology and Defect Structure of the CeO_2(111) Films Grown on Ru(0001) as Studied by Scanning Tunneling Microscopy. *Surf. Sci.* **2006**, *600*, 5004–5010.
15. Knudsen, J.; Merte, L. R.; Grabow, L. C.; Eichhorn, F. M.; Porsgaard, S.; Zeuthen, H.; Vang, R. T.; Lægsgaard, E.; Mavrikakis, M.; Besenbacher, F. Reduction of FeO/Pt(111) Thin Films by Exposure to Atomic Hydrogen. *Surf. Sci.* **2010**, *604*, 11–20.
16. Branda, M. M.; Loschen, C.; Neyman, K. M.; Illas, F. Atomic and Electronic Structure of Cerium Oxide Stepped Model Surfaces. *J. Phys. Chem. C* **2008**, *112*, 17643–17651.
17. Bollinger, M. V.; Lauritsen, J. V.; Jacobsen, K. W.; Nørskov, J. K.; Helveg, S.; Besenbacher, F. One-Dimensional Metallic Edge States in MoS_2. *Phys. Rev. Lett.* **2001**, *87*, 196803.
18. McKenna, K. P.; Shluger, A. L. Electron-Trapping Polycrystalline Materials with Negative Electron Affinity. *Nat. Mater.* **2008**, *7*, 859.
19. Benia, H. M.; Myrach, P.; Gonchar, A.; Risse, T.; Nilius, N.; Freund, H.-J. Electron Trapping in Misfit Dislocations of MgO Thin Films. *Phys. Rev. B* **2010**, *81*, 241415.
20. Freitag, A.; Staemmler, V.; Cappus, D.; Ventrice, C. A.; Al-Shamery, K. A.; Kuhlenbeck, H.; Freund, H. J. Electronic Surface State of NiO(100). *Chem. Phys. Lett.* **1993**, *210*, 10–14.
21. Esch, F.; Fabris, S.; Zhou, L.; Montini, T.; Africh, C.; Fornasiero, P.; Comelli, G.; Rosei, R. Electron Localization Determines Defect Formation on Ceria Substrates. *Science* **2005**, *309*, 752.
22. Fabris, S.; Vicario, G.; Balducci, G.; de Gironcoli, S.; Baroni, S. Electronic and Atomistic Structures of Clean and Reduced Ceria Surfaces. *J. Phys. Chem. B* **2005**, *109*, 22860.
23. Goniakowski, J.; Finocchi, F.; Noguera, C. Polarity of Oxide Surfaces and Nanostructures. *Rep. Prog. Phys.* **2008**, *71*, 016501.
24. Goniakowski, J.; Noguera, C. Polarity at the Nanoscale. *Phys. Rev. B* **2011**, *83*, 115413.
25. Torbrügge, S.; Cranney, M.; Reichling, M. Morphology of Step Structures on CeO_2(111). *Appl. Phys. Lett.* **2008**, *93*, 073112.
26. Duclos, S. J.; Vohra, Y. K.; Ruoff, A. L.; Jayaraman, A.; Espinosa, G. P. High-Pressure X-ray Diffraction Study of

CeO_2 to 70 GPa and Pressure-Induced Phase Transformation from the Fluorite Structure. *Phys. Rev. B* **1998**, *38*, 7755.
27. Engelhardt, J. B.; Dabringhaus, H.; Wandelt, K. Atomic Force Microscopy Study of the CaF_2(111) Surface: from Cleavage *via* Island to Evaporation Topographies. *Surf. Sci.* **2000**, *448*, 187–200.
28. Dabringhaus, H.; Wandelt, K. Theoretical Study of the Adsorption of a CaF_2 Molecule at the (111) Surface of CaF_2 I. Equilibrium Adsorption Positions. *Surf. Sci.* **2003**, *526*, 257–272.
29. Puchin, V. E.; Puchina, A. V.; Huisinga, M.; Reichling, M. Theoretical Modelling of Steps on the CaF_2(111) Surface. *J. Phys.: Condens. Matter* **2001**, *13*, 2081–2094.
30. Jerratsch, J. F.; Shao, X.; Nilius, N.; Freund, H.-J.; Popa, C.; Ganduglia-Pirovano, M. V.; Burow, A. M.; Sauer, J. Electron Localization in Defective Ceria Films: A Study with Scanning-Tunneling Microscopy and Density-Functional Theory. *Phys. Rev. Lett.* **2011**, *106*, 246801.
31. Shao, X.; Jerratsch, J.-F; Nilius, N.; Freund, H.-J. Probing the f States of Ceria by Tunneling Spectroscopy. *Phys. Chem. Chem. Phys.* **2011**, *13*, 12646–12651.
32. Shluger, A. L.; Sushko, P. V.; Kantorovich, L. N. Spectroscopy of Low-Coordinated Surface Sites: Theoretical Study of MgO. *Phys. Rev. B* **1999**, *59*, 2417.
33. Sushko, P. V.; Shluger, A. L.; Catlow, C. R. A. Relative Energies of Surface and Defect States: *Ab Initio* Calculations for the MgO (001) Surface. *Surf. Sci.* **2000**, *450*, 153–170.
34. Bader, R. F. W. *Atoms in molecules: A quantum theory*; Oxford Science: United Kingdom, 1990.
35. Mugarza, A.; Mascaraque, A.; Perez-Dieste, V.; Repain, V.; Rousset, S.; Garcia de Abajo, F. J.; Ortega, J. E. Electron Confinement in Surface States on a Stepped Gold Surface Revealed by Angle-Resolved Photoemission. *Phys. Rev. Lett.* **2001**, *87*, 107601.
36. Schmid, M.; Shishkin, M.; Kresse, G.; Napetschnig, E.; Varga, P.; Kulawik, M.; Nilius, N.; Rust, H.-P.; Freund, H.-J. Oxygen-Deficient Line Defects in an Ultrathin Aluminum Oxide Film. *Phys. Rev. Lett.* **2006**, *97*, 046101.
37. Baron, M.; Bondarchuk, O.; Stacchiola, D.; Shaikhutdinov, S.; Freund, H.-J. Interaction of Gold with Cerium Oxide Supports: CeO_2(111) Thin Films *vs* CeO_x Nanoparticles. *J. Phys. Chem. C* **2009**, *113*, 6042.
38. Mullins, D. R.; Radulovic, P. V.; Overbury, S. H. Ordered Cerium Oxide Thin Films Grown on Ru(0001) and Ni(111). *Surf. Sci.* **1999**, *429*, 186.
39. Kresse, G.; Furthmüller, J. Efficient Iterative Schemes for *Ab Initio* Total-Energy Calculations Using a Plane-Wave Basis Set. *Phys. Rev. B* **1996**, *54*, 11169.
40. Kresse, G.; Hafner, J. *Ab initio* Molecular Dynamics for Liquid Metals. *Phys. Rev. B* **1993**, *47*, 558.
41. Perdew, J. P.; Wang, Y. Accurate and Simple Analytic Representation of the Electron-Gas Correlation Energy. *Phys. Rev. B* **1992**, *45*, 13244.
42. Dudarev, S. L.; Botton, G. A.; Savrasov, S. Y.; Humphreys, C. J.; Sutton, A. P. Electron-Energy-Loss Spectra and the Structural Stability of Nickel Oxide: An LSDA+U Study. *Phys. Rev. B* **1998**, *57*, 1505.
43. Loschen, C.; Carrasco, J.; Neyman, K. M.; Illas, F. First-Principles LDA+U and GGA+U Study of Cerium Oxides: Dependence on the Effective U Parameter. *Phys. Rev. B* **2007**, *75*, 035115.
44. Da Silva, J. L. F.; Ganduglia-Pirovano, M. V.; Sauer, J.; Bayer, V.; Kresse, G. Publisher's Note: Hybrid Functionals Applied to Rare-Earth Oxides: The Example of Ceria. *Phys. Rev. B* **2007**, *75*, 089901.
45. Blöchl, P. E. Projector Augmented-Wave Method. *Phys. Rev. B* **1994**, *50*, 17953.
46. Tersoff, J.; Hamann, D. Theory of the Scanning Tunneling Microscope. *Phys. Rev. B* **1985**, *31*, 805.